03,11,12

Structural and phase features of zinc selenide nanoparticles obtained by laser evaporation

© A.M. Murzakaev, V.V. Osipov, V.V. Platonov

Institute of Electrophysics, Ural Branch, Russian Academy of Sciences,, Yekaterinburg, Russia

E-mail: amurzak@mail.ru

Received May 10, 2022
Revised May 10, 2022
Accepted May 14, 2022

The first production of weakly agglomerated zinc selenide nanopowders by evaporation of a target of the required chemical composition in argon using a fiber ytterbium laser is reported. Nanoparticles have the shape of polyhedrons and, more rarely, spheres with an average size of 18 nm. According to XRD data, the obtained nanopowders contain two phases: a stable cubic phase (sphalerite, 40 wt.%) and a metastable hexagonal phase (wurtzite, 60 wt.%). An analysis of HRTEM showed that most of the nanoparticles have structural defects. Due to superstoichiometry, defects in the crystal structure of the crystallographic shift type are formed in nanoparticles. Magneli phases, Wadsley defects and various kinds of heterogeneity inside the particles were found.

Keywords: Laser evaporation, zinc selenide, nanoparticles, high resolution transmission electron microscopy (HRTEM), defects, phase composition, crystallographic shift, Magnelli phase, Wadsley defects.

DOI: 10.21883/PSS.2022.11.54185.375

1. Introduction

Zinc selenide ZnSe is a typical representative of $A^{II}B^{VI}$ semiconductor compounds and is classified as a compound semiconductor. The first laser with ZnSe doped with *d*-elements was created in 1996 [1], and from that time there is sustained interest in this material [2,3]. Such lasers are promising for monitoring of environment pollution, medicine and other applications. In addition to laser technologies, the important areas of ZnSe use are related to the creation of high-efficiency scintillation detectors used in nuclear physics, biology, medicine and other fields. Under the normal conditions, ZnSe exists in the cubic phase with the sphalerite structure $F\bar{4}3m$ and in the hexagonal phase with the wurtzite structure $P6_3mc$ [4–7]. For brevity, these phases are designated as *s*-ZnSe and *w*-ZnSe respectively. Pure crystals of *w*-ZnSe [8] and *s*-ZnSe [9] were obtained with the *n*- and *p*-type of conduction. Conduction type depends on the method of their making, presence of doping impurities and concentration of own excess components. Crystals with an excess of Zn have the *n*-type conduction, and with an excess of Se — the *p*-type. It is known that ZnSe crystals grown from a melt are characterized by the presence of excess selenium [10]. One of the promising areas is the creation of ceramic active elements from ZnSe nanopowders. Powders of this material, obtained by different methods, have attracted much attention thanks to their scientific and technological significance [11–20]. The laser synthesis method, which consists in the evaporation of a target of the corresponding chemical composition by laser radiation with the intensity of $\sim 1\,\mathrm{MW/cm^2}$ and a high average power and subsequent vapor condensation in the carrier gas flow, makes it possible to obtain weakly agglomerated nanoparticles having an average size of about 10 nm [21,22]. In this case, nanoparticles form during laser flare cooldown within a short time ~ 1 ms, which is accompanied with vortex mixing of vapor and forming pair nanoparticles with the buffer gas flow. It can be stated that the nanoparticle formation conditions are non-equilibrium and can differ from each other in different areas of the laser flare. In this respect, it is important to know the characteristics of obtained nanoparticles, in order to estimate their applicability for different technologies.

The present paper gives the results of a study of the morphology, structural and phase peculiarities of the ZnSe nanopowder, obtained using a fiber ytterbium laser, both at the level of individual nanoparticles and the whole nanopowder.

2. Materials, preparation and study methods

2.1. Nanoparticle preparation procedure

Nanopowders were prepared using an experimental unit [22,23] improved as regards the nanopowder collection method. Targets were evaporated using the focused radiation of a fiber ytterbium laser LS-07N. The lens focal length was increased to 600 mm in order to reduce spattering of micron melt droplets from the crater, and the laser operated in the pulse-periodic mode. The duration of rectangular radiation pulses and their repetition period were 120 and 240 μs. Radiation intensity on the target at the pulse power of 600 W was $0.18\,\mathrm{MW/cm^2}$. The target was rotated and moved both in the horizontal and in the vertical direction to ensure uniform evaporation. The nanopowder

was prepared in argon supplied to the unit from a cylinder with the volume flow rate of $\approx 3.7\,m^3/h$. Gas pressure in the evaporation chamber was approximately equal to the atmosphere air pressure. The forming nanoparticles, as well as micron and submicron melt droplets and target debris were transferred with the argon flow from the evaporation chamber into cyclone separators for trapping of large particles. Then the aerosol flow was passed through a hose filter where most nanoparticles settled. The gas was discharged to the atmosphere after additional purification. The nanopowder was collected from the hose filter by vibration of the filtering hose.

The target material was ZnSe micropowder with the main substance content of 99.9 wt.%. The powders were pressed by a one-axle press into cylindrical compact sets which were sintered in H_2 flow at 930°C.

2.2. Nanoparticle analysis methods

The research was conducted using ZnSe nanopowders without any treatment in order to obtain ceramics. Their specific surface was measured by means of the BET method using a TriStar 3000 V6.03 A device. X-ray diffraction analysis was performed using a D8 DISCOVER diffractometer in Cu radiation ($K_{\alpha 1,2}$, $\lambda = 1.542$ Å) using the TOPAS 3 software. The elemental analysis of the nanopowders was performed by the emission-spectral approach with inductively-coupled plasma (ICP-AES) using an Optima 2100 spectrometer.

The morphology and phase composition of nanoparticles were studied by transmission electron microscopy (TEM), selected area electron diffraction (SAED) and high-resolution transmission electron microscopy (HRTEM) using a JEM 2100 device. The device resolution by points was 0.19 nm, and by lines — 0.14 nm. The image was recorded using a Gatan camera. Calibration of TEM magnification and determination of the device constant for electron diffraction measurements were performed using gold foil. Images were processed and analyzed using the Gatan Digital Micrograph software, which made it possible to calibrate the images, as well as to apply masks and filters for the Fourier transformations both of the whole image and selected areas of the image, to perform measurements and save data in different formats. The Fourier masks help eliminate the unwanted noise or improve the periodic image elements. The values of interplanar distances for different sample phases were taken from the powder diffraction file (PDF).

3. Results and discussion

3.1. Specific surface, chemical analysis and X-ray diffraction analysis

The performance of nanopowder preparation was 100 g/h. The nanopowder specific surface, determined by the BET method, was equal to $47\,m^2/g$.

Table 1. Chemical composition of the initial micropowder, target and the prepared nanopowder. Relative error of element content determination −3%

Sample	Atomic content of elements, at.%		Chemical formula
	Zn	Se	
Initial ZnSe micropowder	46.8	53.2	$ZnSe_{1.14}$
ZnSe target	46.9	53.1	$ZnSe_{1.13}$
ZnSe nanopowder	47.2	52.8	$ZnSe_{1.12}$

The results of chemical composition analyses for the initial micropowder, prepared target and nanopowder are given in Table 1. According to the analysis results, the initial zinc selenide powder contains a small excess of selenium. The content of Zn and Se atoms in the initial target and in the nanopowder within the relative measurement error of 3% almost coincides with the composition of the initial ZnSe micropowder.

Table 2 gives the results of X-ray diffraction analysis of the target before evaporation and the prepared nanopowder. ZnSe in the initial target has mainly a stable cubic crystal lattice s-ZnSe, the metastable hexagonal phase (w-ZnSe) is present only in the form of traces (1 wt.%). The metastable phase content in the prepared nanopowder increases to 60 wt.%, while the content of the stable phase s-ZnSe decreases respectively. The determined parameter of the ZnSe hexagonal crystal lattice both in the target and in the nanopowder differ from the published data, which means the presence of defects in it, including those related to deviations from the ZnSe stoichiometry. The latter correlates with the elemental analysis data on an excessive selenium content in the target and in the prepared nanopowder.

The formation of a metastable crystal lattice in nanoparticles, obtained by means of a powerful laser, has been already observed earlier. For instance, when a CO_2 or fiber ytterbium laser is used, the formation of a metastable (monoclinic) phase in yttrium oxide nanoparticles in [21,22] is associated with the fast cooldown of nanoparticles, forming in the laser flare, for minimum 1 ms. The hexagonal phase in ZnSe nanoparticles, most probably, forms due to the same reason. These considerations agree with the fact that ZnSe nanoparticles, obtained in the air using a femtosecond laser, have only a hexagonal crystal lattice and do not contain a cubic phase [20]. The absence of a cubic phase in nanopowders obtained with the use of a femtosecond laser is, apparently, conditioned by a faster (than in our case) cooldown of vapor and nanoparticles in the laser flare. It should be noted that the mechanism of target ablation by a quasicontinuous ytterbium laser and a femtosecond laser, as well as the conditions of nanoparticle cooldown in the laser flare considerably differ from each

Table 2. Results of X-ray diffraction analysis of the ZnSe target and the prepared nanopowder: lattice constants, sizes of coherent scattering regions (CHR) and percentage of phases

Sample	*s*-ZnSe ($F\bar{4}3m$, PDF № 00-037-1463, $a = 5.6688$ Å)			*w*-ZnSe ($P6_3mc$, PDF № 01-089-2940, $a = 3.996$ Å, $c = 6.626$ Å)		
	Lattice parameters, Å	CHR, CHR, nm	Content, wt.%	Lattice parameters, Å	CHR, CHR, nm	Content, wt.%
ZnSe target	$a = 5.6696$	> 200	99	$a = 3.950$, $c = 6.640$	–	1
ZnSe nanopowder	$a = 5.6690$	21	40	$a = 3.999$, $c = 6.579$	17	60

other. In the case of an ytterbium laser, the matter is removed from the target mainly in the form of vapor from the pool of the liquid melt in the crater during a radiation action with the intensity of $\sim 10^6$ W/cm^2. On the contrary, under the action of a femtosecond laser pulse with the intensity of $\sim 10^{12}$ W/cm^2 the matter is removed after its end in the form of a mixture of vapor and droplets of the melt.

3.2. Nanoparticle morphology

Fig. 1 shows a typical photograph of ZnSe nanoparticles obtained by means of TEM. The nanopowder consists of both individual nanoparticles and nanoparticles in aggregates. Particle sizes are from 2 to 70 nm. Most nanoparticles have the shape of regular and irregular polyhedrons, which differs them from the laser-generated nanoparticles of refractory oxides, which usually have a nearly spherical shape [21,22]. Nanoparticles with a hexagonal faceting occur rarely. Some large particles have a striped appearance, which may mean twinning in them. The HRTEM images

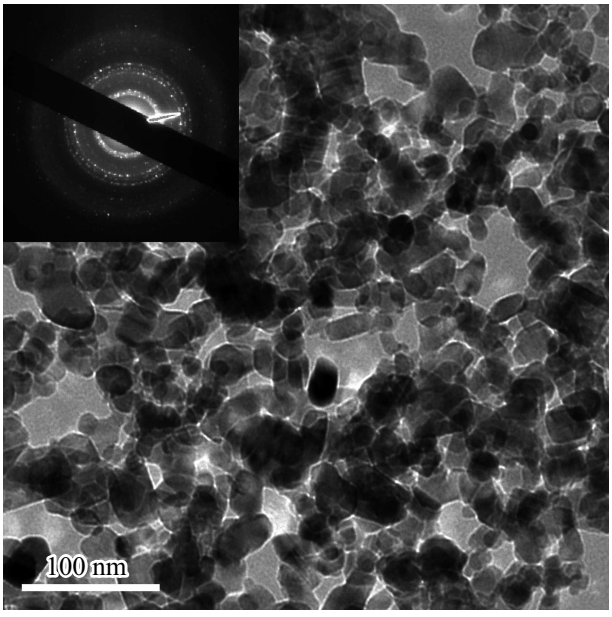

Figure 1. Typical bright-field image of ZnSe nanoparticles, the inset shows an electron-diffraction pattern of ZnSe nanoparticles.

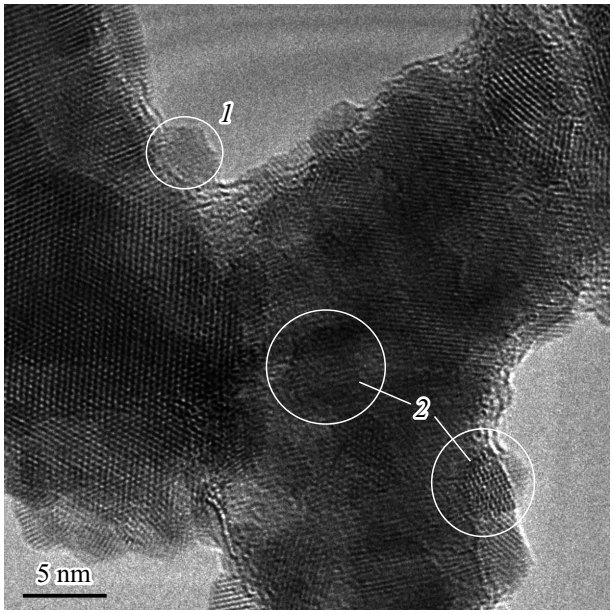

Figure 2. Amorphous (*1*) and crystalline (*2*) ZnSe nanoparticles.

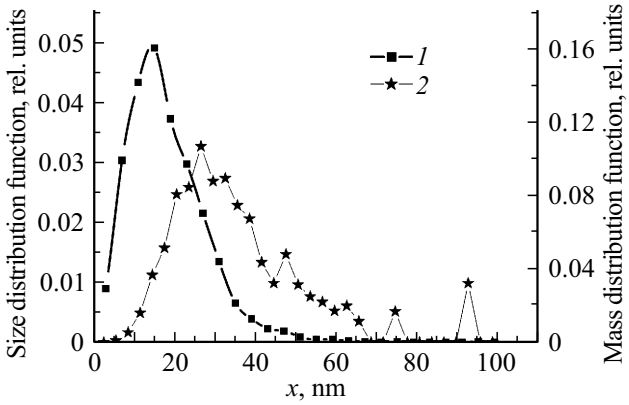

Figure 3. Size (*1*) and weight (*2*) distribution of ZnSe nanoparticles.

(Fig. 2) show that on the surface and inside the sample particles there are both quasi-spherical amorphous (shown by circle *1*) and crystalline (shown by circle *2*) nanoparticles of a close size (2–5 nm). The nanoparticle size distri-

bution was plotted by the measurement of 2000 particles, each of which was measured in two directions, and the measurement results were averaged. The shape of the ZnSe nanoparticle size distribution function is close to a logarithmically normal distribution (Fig. 3, curve *1*), the average arithmetic size of nanoparticles was equal to 18 nm. At the same time, the nanoparticle weight distribution was considerably shifted towards larger sizes (Fig. 3, curve *2*), and a significant contribution is made by the weight of an occasional number of nanoparticles sized more than 60 nm. Accordingly, the total weight of nanoparticles sized more than 30 nm was 62 wt.% from the total particle weight.

3.3. Analysis of electron diffraction patterns

Research of ZnSe nanoparticles by the SAED method, as distinct from X-ray diffraction analysis, allows for studying of their crystal structure within the microscope field sized slightly more than 100 nm, where only several tens of particles are located. Fig. 1 shows the nanoparticle photograph and the inset in Fig. 1 shows the electron diffraction pattern. The electron diffraction patterns of nanoparticles consist of rings and spots due to the contributions of nanosized crystals. Diffraction patterns for the chosen regions have confirmed the nanoparticle crystal structure which was identified as a hexagonal w-ZnSe structure with the unit cell parameters $a = b = 0.39$ nm, $c = 0.65$ nm. Some points could be identified as a cubic c-ZnSe structure with the unit cell parameter $a = 0.56$ nm. Additional points with a very low intensity, in addition to the main interpreted diffraction rings and points, have been found in certain electron diffraction patterns of the highlighted areas. The interplanar distances calculated according to these spots correspond to the selenium structure within the measurement error. Almost all the electron diffraction patterns have a low-observable halo on the background of the main bright reflections.

3.4. Analysis of HRTEM patterns

We have performed detailed studies of the structure and phase composition of a large number of individual ZnSe nanoparticles of different sizes. The HRTEM images were analyzed according to the following scheme in order to determine the crystal structure of individual nanoparticles and areas of nanoparticles in the straight space. 1) A fast Fourier transformation (FFT) of the whole pattern or a highlighted area of the HRTEM image equivalent to electronic diffraction is calculated. The two-dimensional spectrum of FFT of the highlighted central area of the direct-resolution pattern for the particle crystal lattice is shown in the inset in Fig. 4. 2) Then, the FFT is analyzed and interplanar distances are determined. 3) The obtained values of interplanar distances are compared with the database and a conclusion on the nanoparticle phase composition is made.

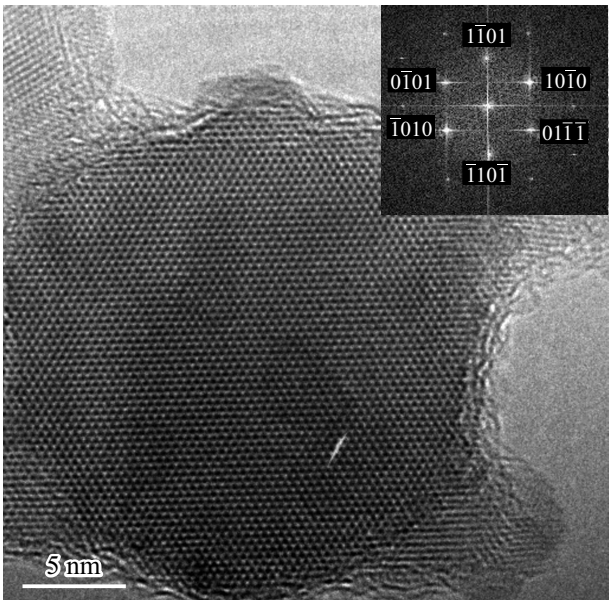

Figure 4. HRTEM-images of ZnSe nanoparticles, the inset shows the FFT of the highlighted area.

The HRTEM-images have shown that almost all the particles are crystalline. There are individual amorphous particles smaller than 3–4 nm. The surface of larger nanoparticles also has a low-observable amorphous interlayer. The results of the analysis of the atomic resolution patterns for individual ZnSe nanoparticles can be conventionally subdivided into several groups which will be discussed below.

Fig. 4 shows a typical HRTEM-image of a ZnSe nanoparticle of a not very smooth spherical shape. The nanoparticle diameter is about 25 nm. A distinct six-fold symmetry was observed in the FFT pattern — „electronic diffraction“ of the highlighted area. The crystal structure of the ZnSe nanoparticle has been identified as w-ZnSe by an analysis of the distances and angles between the points (see the inset in Fig. 4).

The results shown in Fig. 5 were obtained after an analysis of the area of the overall pattern highlighted by a square *1*. The FFT pattern for the highlighted area is shown in the inset *2*. After applying ring masks onto the FFT pattern (inset *3*) and an inverse Fourier transformation (IFT) (inset *4*), we have obtained the location pattern of the w-ZnSe phase with the interplanar distance $d_{100} = 0.345$ nm and monoclinic Se phase with $d_{014} = 0.275$ nm. The region containing pure selenium is highlighted by an oval in area *1*.

Fig. 6, *a* shows the HRTEM image of ZnSe nanoparticles. The FFT sample corresponding to the whole pattern is shown in the inset in Fig. 6, *a* and confirms the crystalline nature of the particles. The results obtained after the FFT pattern interpretation confirm the presence of a stable cubic s-ZnSe structure with the interplanar distance $d_{111} = 0.327$ nm and metastable hexagonal w-ZnSe

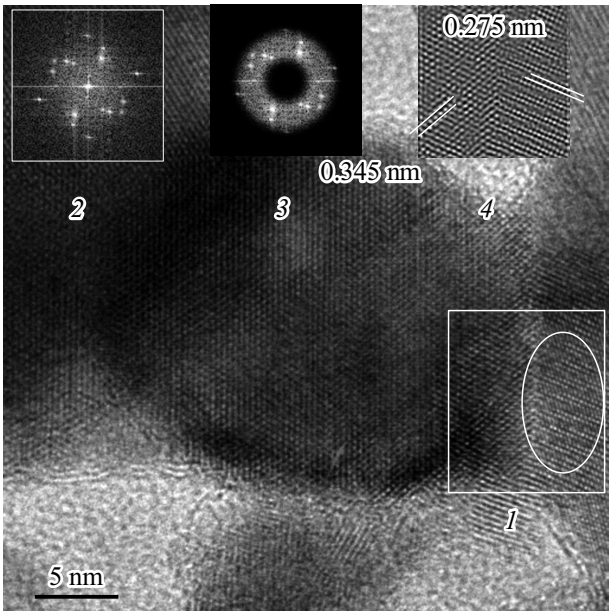

Figure 5. HRTEM-images of ZnSe nanoparticles, the insets show: *1* — analyzed area, *2* — FFT of the highlighted area, *3* — mask, *4* — areas containing ZnSe and Se.

structure with $d_{100} = 0.343$ nm. The location pattern of the cubic phase (Fig. 6, *b*) was obtained after the application of ring masks onto the FFT pattern (points *1, 2, 3, 4*) and IFT. The location pattern of the hexagonal phase (Fig. 6, *c*) was obtained after the application of ring masks onto the FFT pattern (highlighted by a white circle) and IFT.

Fig. 7, *a* shows the HRTEM image of ZnSe nanoparticles. The FFT sample corresponding to the whole pattern is shown in the inset in Fig. 7, *a*. Special attention was paid to the brightest and widest points *1* and *2*. The result obtained after the interpretation of the FFT pattern for these points corresponds to the interplanar distance of 0.333 nm. This interplanar distance value is absent in the powder diffraction files (PDF). An additional analysis of these points was performed by applying diametrically opposite point masks. A pattern of this phase in the form of parallel bands can be obtained by inversion. A part of this phase in Fig. 7, *a* is highlighted by a white rectangle. In addition, the interplanar distance values were obtained from the intensity profiles (Fig. 7, *b*). It has turned out that the interplanar distances, determined from the intensity profile, do not match the interplanar distance value initially determined from the interpretation of the FFT from points *1* and *2*. The distance between the first and second layer, $d = 0.343$ nm, corresponds to *w*-ZnSe with $d_{100} = 0.343$ nm. The distance between the second and third layer, $d = 0.273$ nm, corresponds to Se. The distances between the third to eighth layers, $d = 0.343$ nm, correspond to *w*-ZnSe, while the distances between the eighth and ninth layers, $d = 0.274$ nm, correspond to Se. In total, the ten first layers have the thickness of 3.279 nm. The average interplanar distance is $3.279\,\text{nm}/10 = 0.3279$ nm. The measured 30 first interplanar distances, along with a large number of interplanar distances corresponding to *w*-ZnSe with $d_{100} = 0.343$ nm, include interplanar distances equal to $d = 0.273$ nm which correspond to Se. The average interplanar distance for 20 layers is $6.627\,\text{nm}/20 = 0.3314$ nm, and for 30 layers — $9.975\,\text{nm}/30 = 0.3325$ nm. It means that a particle has the *w*-ZnSe structure with embedded planes of pure Se.

The distance between such individual bands for a perfect crystal must be strictly identical. This defective structure greatly resembles the structure of non-stoichiometric oxides. The structural formation principles of phases of certain oxides under oxygen deficit (shortage) were formulated by Magneli et al. [24], Wadsley [25] and other researchers [26,27] who suggested the term „crystallographic shear" (CS), meaning a hypothetical operation which leads to the formation of defects of a certain type. Oxides with oxygen deficit consist of regions with a perfect structure of a stoichiometric oxide with separated planes of crystallographic shear (CS-planes), which are thin „lamellar" crystal regions with a different structure and composition. The oxygen deficit present in the whole crystal is „concentrated" in this CS-planes. Similarly to that, we can also affirm that ZnSe nanoparticles have the *w*-ZnSe structure with $d_{100} = 0.343$ nm and additional CS-planes of Se.

Crystallographic shear structures were studied by X-ray diffraction methods [22–24]. However, this method in the case of nanoparticles becomes less sensitive due to line widening. Diffraction methods (X-ray, neutron, neutron electronic diffraction) used in crystallographic studies give an averaged pattern of the crystal structure. The averaged pattern (structure) is close to the true structure when studying high-purity crystals or crystals containing relatively few defects. However, an averaged pattern in case of non-stoichiometric and defective crystals can give a very poor and even an incorrect idea of the actual structure in the defect region. This proves the need for the application of experimental methods sensitive to the local structure.

High-resolution electron microscopy was usually limited to the determination of lattice parameters and space groups for crystals of a very small size, as well as to the study of dislocations and packing defects. However, the method of direct lattice imaging turned out to be extremely fruitful in the study of the CS-plan structure. Such images usually have the shape of „fringes" or parallel bands which correspond to the position of atoms having the strongest reflectance. Distances between individual bands for a perfect crystal must be strictly identical, however, the corresponding image in case of a CS-plane has an irregularity in the location of bands. Thus, a pair of bands, located in relation to each other with a different interplanar distance value than in the normal crystal region, means a shear plane. This method is certainly very useful in the study of defects in shear structures.

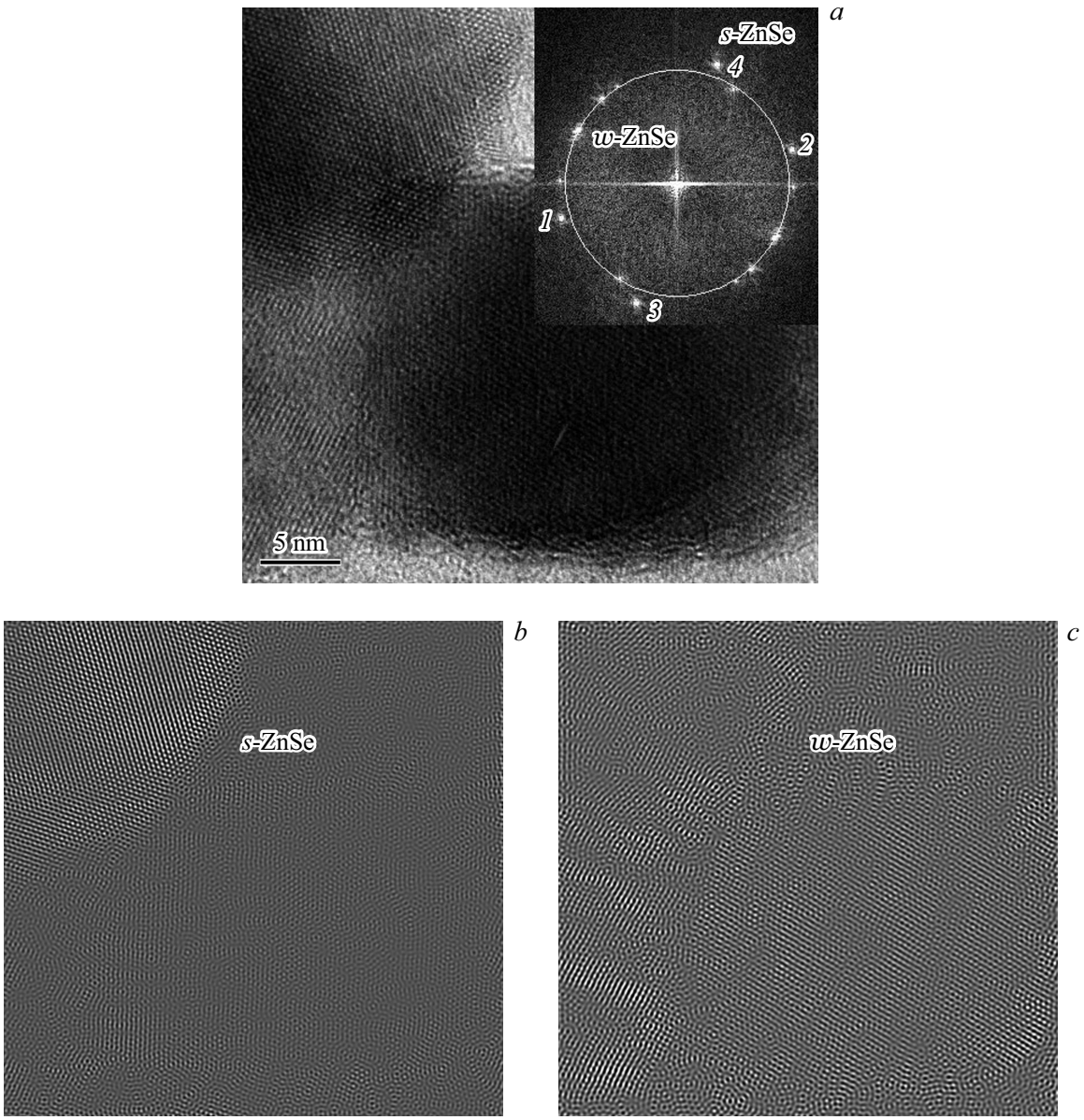

Figure 6. HRTEM images of ZnSe nanoparticles (*a*, the inset shows the FFT, ZnSe „nanoparticle electron diffraction pattern"), a particle with the cubic phase (*b*), particles with the hexagonal phase (*c*).

An analysis of many HRTEM patterns for nanoparticles has shown that most nanoparticles have such a defective structure. CS-planes in most of the studied ZnSe nanoparticles remain in a solid solution, but are located chaotically in the structure. It means that these nanoparticles have the Wadsley defects with chaotically distributed planes of crystalline shear among the normal packing. The Magneli phases of a different compositions have been also found among the ZnSe nanoparticles (regular alternation of the CS-plane and normal packing as in Fig. 8).

Crystallographic shear structures in some ZnSe nanoparticles form two mutually intercrossing sets of planes. As a result, regions with a perfect structure are not infinite layers but blocks. Such „block" structures, also called double shear structures, retain the length, width and method of block connection typical for a non-stoichiometric ZnSe structure (Fig. 8). The complexity of block phases rises sharply if the structure is composed of blocks of two or three different sizes, joining in a certain order, instead of same-size blocks.

In principle, there can be structures composed of three sets of CS-planes and, consequently, structure blocks which have a finite and small size in all the three dimensions. These three sets of CS-planes can be mutually orthogonal or be located at different angles depending on the crystal structure of the studied samples. The samples must be inclined to angles over 60° in order to reveal them (obtain their patterns). However, we have not yet found mating of this

type due to the design features of the ultrahigh resolution objective lens of HRTEM, for which the permissible sample inclination angle is maximum 20°. From this viewpoint, ZnSe nanoparticles must be studied in more detail by high-resolution microscopy using a „metallographic“ transmission electron microscope. They might help reveal the structural peculiarities of nanoparticle formation.

So, ZnSe solid solutions with a Se excess in fact have a heterogeneous structure at the microlevel. The direct experimental evidence of such microheterogeneity is the presence of the Magneli phases and Wadsley defects. These are vivid examples of microheterogeneity, since they differ both in structure and composition from the other regions of the solid solution where they are contained. The formation of such crystal structure defects in laser-generated ZnSe nanoparticles can be related to the sharply non-equilibrium conditions of their formation. In particular, to the very fast cooldown of the vapor and forming nanoparticles in the laser flare during its propagation into argon, which is accompanied with their vortex mixing.

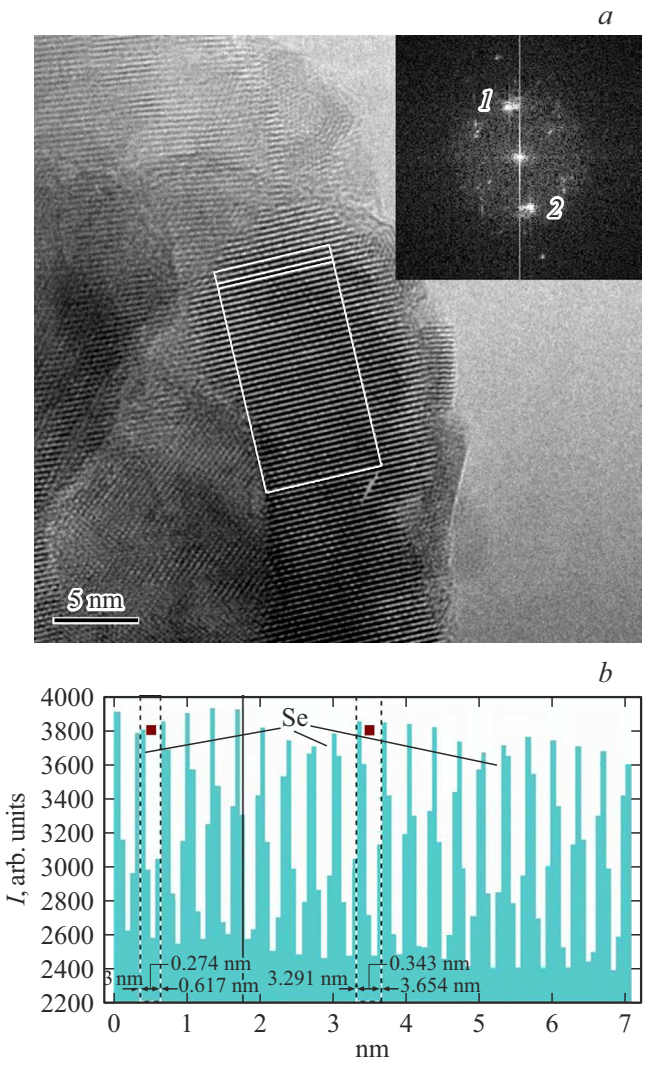

Figure 7. *a* — HRTEM images of ZnSe nanoparticles, the inset shows the FFT of the whole pattern, *b* — intensity profile of the particle area.

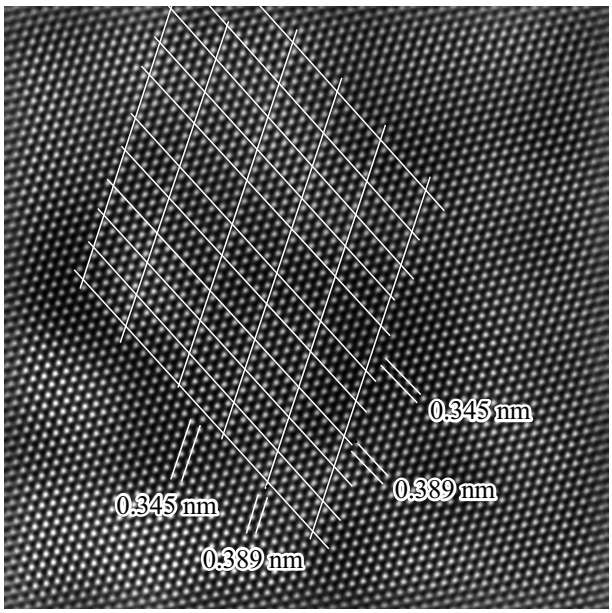

Figure 8. HRTEM pattern of the double shear structure typical for the non-stoichiometric ZnSe structure.

4. Conclusions

Thus, the following conclusions can be made according to the research results.

1. ZnSe nanopowder containing weakly agglomerated particles in the shape of polyhedrons sized 2−70 nm has been prepared for the first time using a fiber ytterbium laser. Their average arithmetic size was ∼ 18 nm. According to the X-ray diffraction analysis results, the nanopowders have a cubic (40 wt.%) and a hexagonal (60 wt.%) crystalline phases of ZnSe. The method of selected area electron diffraction has detected a very small amount of the selenium phase, which could not be detected by X-ray diffraction analysis.

2. The correlation between the content of zinc and selenium atoms in the prepared ZnSe nanopowders is virtually the same as the correlation in the initial target thanks to the congruent evaporation of this material.

3. The nanoparticles generated by the laser ablation method form in the course of very fast cooldown and condensation of vapor during its vortex mixing with the buffer gas flow. Amorphous nanoparticles sized up to 5 nm form in the nanopowder obtained under these conditions, while larger ones have a crystalline structure. The analysis of HRTEM has shown that the particles have heterogeneities in the chemical composition and various crystalline structure defects at the micro- and nanolevel, which cannot be studied by X-ray diffraction analysis. Defects (crystallographic

shear) of the crystalline structure form in nanoparticles due to hyperstoichiometry (excess) of selenium. The Magneli phases (regular alternation of the crystallographic shear plane and normal packing) and Wadsley defects (chaotically distributed crystallographic shear planes among the normal packing), as well as various heterogeneities inside nanoparticles were detected.

Acknowledgments

The authors would like to thank V.A. Shitov (Institute of Electrophysics of the Ural Branch of RAS) and A.V. Abramov (Institute of Physics and Technology of UrFU) for the making of targets for evaporation, D.G. Lisienko (Institute of Physics and Technology of UrFU) for the fulfillment of the elemental analysis of target samples and nanopowders, T.M. Demin (Institute of Electrophysics of the Ural Branch of RAS) for texture studies, A.I. Medvedev (Institute of Electrophysics of the Ural Branch of RAS) for XFA. TEM and HRTEM studies, X-ray diffraction analysis and specific surface analysis were performed using the equipment of the Core Shared Research Facility at the Institute of Electrophysics of the Ural Branch of RAS.

Funding

The work has been performed under grant of the Russian Science Foundation No. 22-29-20039.

Conflict of interest

The authors declare that they have no conflict of interest.

References

[1] R.H. Page, L.D. De Loach, K.I. Shaffers, F.D. Patel, R.J. Beach, S.A. Payne, W.F. Krupke, A. Burger. Recent developments in Cr^{2+}-doped II–VI compound lasers. In: Advanced Solid-State Lasers, 1996 Technical Digest. Optical Society of America, Washington DC (1996). P. 246.
[2] S.B. Mirov, V.V. Fedorov, D.V. Martyshkin, I.S. Moskalev, M.S. Mirov, V.P. Gapontsev. Opt. Mater. Express **1**, *5*, 898 (2011).
[3] K.N. Firsov, T.M. Gavrishchuk, V.B. Ikonnikov, S.Y. Kazantsev, I.G. Kononov, T.V. Kotereva, N.A. Timofeeva. Laser Phys. Lett. **13**, *5*, 055002 (2016).
[4] Fizika i khimiya soedineniy $A^{II}B^{VI}$ / pod red. M. Aven, D.S. Prener. Mir, M. (1970). 624 s. (in Russian).
[5] M.P. Kulakov, V.D. Kulakovsky, I.B. Savchenko, A.V. Fadeev. FTT **18**, 909 (1976) (in Russian).
[6] L.T. Steinberger. Prog. Cryst. Growth Charact. Mater. **7**, *1–4*, 7 (1983).
[7] S.D. Scott, H.L. Barnes. Geochim. Cosmochim. Acta **36**, *11*, 1275 (1972).
[8] J.F. Wang, A. Omino, M. Isshiki. J. Cryst. Growth **229**, *1*, 69 (2001).
[9] T.S. Kim, Y.J. Shin, T.S. Jeong, C.T. Choi, P.Y. Yu, K.J. Hong. J. Korean Phys. Soc. **38**, *1*, 47 (2001).
[10] T. Khanh, E. Mozhevitina, A. Khomyakov, R. Avetisov, A. Davydov, V. Chegnov, V. Antonov, S. Kobeleva, N. Zhavoronkov, I. Avetissov. J. Cryst. Growth **457**, 331 (2017).
[11] J.R. Macdonald, S.J. Beecher, A. Lancaster, P.A. Berry, K.L. Schepler, S.B. Mirov, A.K. Kar. Opt. Express **22**, *6*, 7052 (2014).
[12] S. Vasilyev, I. Moskalev, M. Mirov, V. Smolsky, S. Mirov, V. Gapontsev. Laser Tech. J. **13**, *4*, 24 (2016).
[13] A.B. Panda, S. Acharya, S. Efrima, Y. Golan, Y. Golan. Langmuir **23**, *2*, 765 (2007).
[14] W. Zhou, R. Liu, D. Tang, X. Wang, H. Fan, A. Pan, Q. Zhang, Q. Wan, B. Zou. Nanotechnology **24**, *5*, 055201 (2013).
[15] H. Li, B. Wang, L.J. Li. J. Alloy. Compd. **506**, *1*, 327 (2010).
[16] B. Feng, J. Cao, D. Han, S. Yang, J. Yang. J. Mater. Sci: Mater. Electron. **26**, *5*, 3206 (2015).
[17] J.H. Bang, K.S. Suslick. Adv. Mater. **22**, *10*, 1039 (2010).
[18] E. Mosquera, N. Carvajal. Mater. Lett. **129**, 8 (2014).
[19] K.V. Anikin, N.N. Melnik, A.V. Simakin, G.A. Shafeev, V.V. Voronov, A.G. Vitukhnovsky. Chem. Phys. Lett. **366**, *3–4*, 357 (2002).
[20] H.I. Wang, W.T. Tang, L.W. Liao, P.S. Tseng, C.W. Luo, C.S. Yang, T. Kobayashi. J. Nanomater. **2012**, Article ID 278364 (2012).
[21] V.V. Osipov, V.V. Platonov, V.V. Lisenkov. In: Handbook of Nanoparticles / Ed. M. Aliofkhazraei. Springer International Publishing, Cham (2016). P. 633.
[22] V.V. Osipov, V.V. Platonov, V.V. Lisenkov, E.V. Tikhonov. Fizika i khimiya obrabotki materialov **5**, 5 (2021) (in Russian).
[23] V.V. Osipov, V.V. Platonov, V.V. Lisenkov, E.V. Tikhonov, A.V. Podkin. Appl. Phys. A **124**, *1*, article 3 (2018).
[24] J.S. Andersson, B. Collén, U. Kuylenstierna, A. Magnéli. Acta Chem. Scand. **11**, 1641 (1957).
[25] A.D. Wadsley. In: Non-Stoichiometric Compounds / Ed. L. Mandelcorn. Academic Press, N.Y. (1964). P. 98.
[26] J.S. Anderson, B.G. Hyde. J. Phys. Chem. Solids **28**, *8*, 1393 (1967).
[27] L.A. Bursill, B.G. Hyde. Prog. Solid State Chem. **7**, 177 (1972).